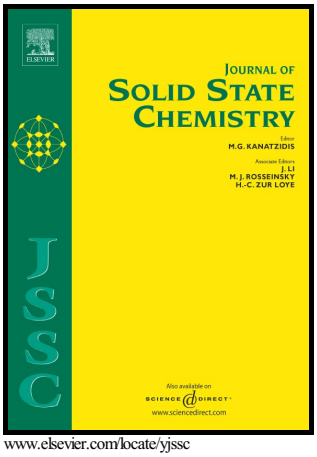

www.elsevier.com/locate/yjssc

Perovskite solid solutions $La_{0.75}Bi_{0.25}Fe_{1-x}Cr_xO_3$: preparation, structural, and magnetic properties

S.A. Ivanov, P. Beran, G. Bazuev, R. Tellgren, T. Sarkar, P. Nordblad, R. Mathieu

PII: S0022-4596(17)30252-9
DOI: http://dx.doi.org/10.1016/j.jssc.2017.06.031
Reference: YJSSC19849

To appear in: *Journal of Solid State Chemistry*

Received date: 21 May 2017
Revised date: 27 June 2017
Accepted date: 30 June 2017

Cite this article as: S.A. Ivanov, P. Beran, G. Bazuev, R. Tellgren, T. Sarkar, P. Nordblad and R. Mathieu, Perovskite solid solutions $La_{0.75}Bi_{0.25}Fe_{1-x}Cr_xO_3$ preparation, structural, and magnetic properties, *Journal of Solid Stat Chemistry,* http://dx.doi.org/10.1016/j.jssc.2017.06.031

Perovskite solid solutions $La_{0.75}Bi_{0.25}Fe_{1-x}Cr_xO_3$: preparation, structural, and magnetic properties

S. A. Ivanov[a,b], P. Beran[c], G. Bazuev[d], R. Tellgren[e], T. Sarkar[b], P. Nordblad[b], R. Mathieu[b]

[a]Department of Inorganic Materials, Karpov' Institute of Physical Chemistry, 105064 Moscow, Russia

[b]Department of Engineering Sciences, Box 534, Uppsala University, SE-751 21 Uppsala, Sweden

[c]Nuclear Physics Institute of the CAS, Hlavni 130, 250 68 Řež, Czech Republic

[d]Institute of Solid State Chemistry, Ural Branch of the Russian Academy of Sciences, 620990, Ekaterinburg, Russia

[e]Department of Chemistry, Angström Laboratory, Uppsala University, Box 538, SE-751 21 Uppsala, Sweden

Abstract

Solid solutions of $La_{0.75}Bi_{0.25}Fe_{1-x}Cr_xO_3$ (x = 0.1, 0.25, 0.5, and 0.75) prepared by conventional solid state reaction have been studied by means of X-ray powder diffraction (XRPD), neutron powder diffraction (NPD) and magnetic measurements. The NPD and XRPD patterns indicate orthorhombic structure (space group *Pnma*) for all compositions in the whole temperature range investigated (4-900 K). The lattice parameters of $La_{0.75}Bi_{0.25}Fe_{1-x}Cr_xO_3$ were found to decrease with the Cr content. It was established that the Fe^{3+} and Cr^{3+} cations are randomly positioned at the *B*-site of the perovskite structure.

All samples order antiferromagnetically below transition temperatures that decrease with increasing Cr content, from around 700 K for x = 0.1 to about 300 K for x = 0.75. The antiferromagnetic arrangement of the Fe^{3+}/Cr^{3+} magnetic moments in the *B*-site is of *G*-type along the *x*-axis (*Gx* mode) with propagation vector k = (0,0,0) for all concentrations of Cr. Effects of the composition on several structural distortion parameters were investigated and an anomalous variation of the octahedral deformation with Cr content was found. Whilst the overall octahedral deformation varies irregularly with increasing Cr content, the octahedral tilting was found to decrease monotoneously.

Graphical abstract

Left: Representations of the (top) crystal and (bottom) magnetic structure of $La_{0.75}Bi_{0.25}Fe_{1-x}Cr_xO_3$.
Right: Temperature dependence of the Fe/Cr-site magnetic moment extracted from NPD data.

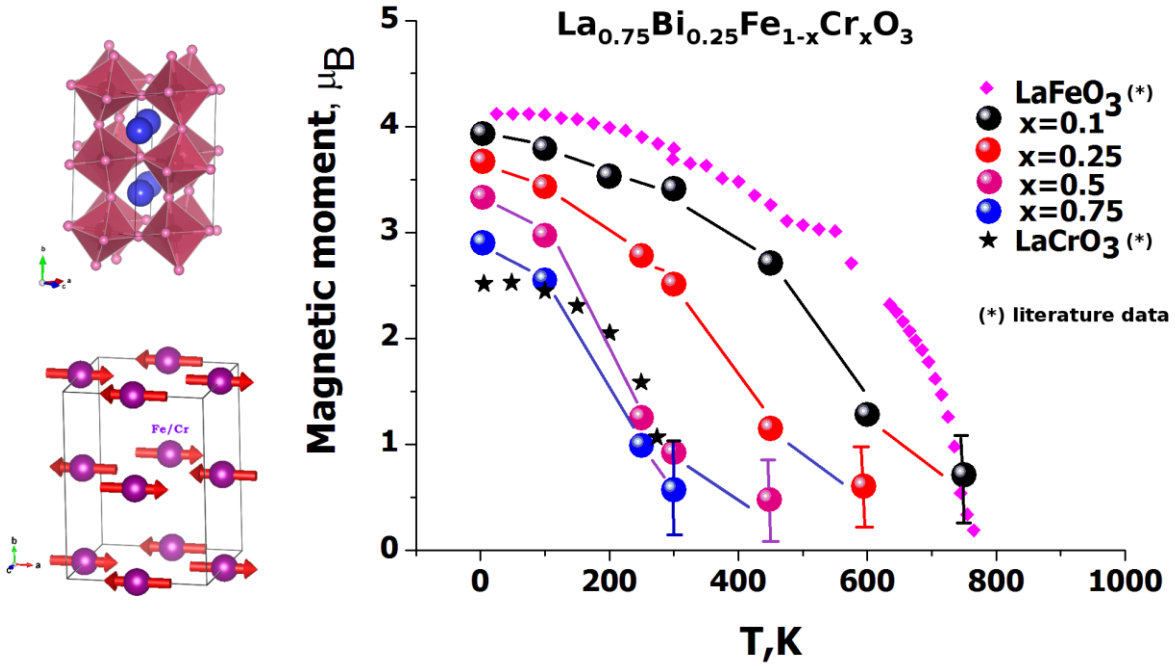

Keywords: A. Ceramics; A. Electronic materials; C. Neutron scattering; C. X-ray diffraction; D. Crystal structure; D. Magnetic properties.

1. Introduction

Complex metal oxides with perovskite-related structure have been of interest the last several decades due to the structural versatility of the perovskite lattice and remarkable properties originating from interplay between spin, charge, and orbital degrees of freedom [1-3]. Because of their highly tunable physical and chemical properties, these compounds offer opportunities to study new physical phenomena and they also provide materials for technological advances [4-6]. In this context, multiferroic (MF) materials are promising for applications in fields such as spintronics and non-volatile data storage [7-12]. Multiferroic double perovskites $A_2B'B''O_6$, in which two different *B*-site cations form a superlattice within the ABO_3 perovskite structure, have recently attracted substantial interest as MF candidate materials [13-18]. This interest was sparked by the prediction of ferromagnetism and ferroelectricity in Bi_2FeCrO_6 (BFCO) of magnitudes (magnetic moment of 2 μ_B/f.u. and a polarization of 80 mC/cm^2) well beyond the values earlier reported for MF materials [16-17]. The successful growth of BFCO, a double perovskite with ferromagnetic and ferroelectric properties well above room temperature, opened opportunities for practical applications of MF. Substantial work has been conducted on BFCO to further improve its magnetic properties, such as doping on the A or B sites. However, the role of doping on the magnetic properties is not completely clear and requires further investigation [19].
The rare-earth (*R*) ferrites, chromites, and several other perovskite compositions with Fe and Cr combinations in the *B*-site are important families of functional materials [20-25]. Recently, these materials were reported to exhibit promising MF properties that are tunable by structural and compositional parameters [26, 27]. Most $RFeO_3$ compounds have a similar distorted orthorhombic perovskite structure of space group *Pnma* and order antiferromagnetically with Néel temperatures (T_N) varying from 620 K to 750 K[28]. The Fe^{3+} magnetic moments in $RFeO_3$ are arranged in a canted *G*-type antiferromagnetic (AFM) structure [29]. Multiferroic properties of $LaFeO_3$ were reported [26,27], including ferroelasticity at room temperature

[30,31]. The AFM ordering of Cr^{3+} ions in rare earth orthochromites ($RCrO_3$) is below or near room temperature ($T_N \sim 100–300$ K) [22].

Earlier studies indicate that the mixture of Fe and Cr cations on the *B*-site in $RFe_{1-x}Cr_xO_3$ perovskites promotes ferromagnetic (FM) coupling [32] due to the superexchange effect of orderly arranged $Fe(d^5)$–O–$Cr(d^3)$ bonds [33,34]. Most of the investigated Fe/Cr perovskites are, however, found to be disordered with random distribution of Fe^{3+} and Cr^{3+} ions at the *B*-sites [35-37]. The presence of disorder in the *B*-site gives rise to a mixture of Fe^{3+}-O-Fe^{3+}, Cr^{3+}-O-Cr^{3+}, and Fe^{3+}-O-Cr^{3+} interactions. Table 1 lists some magnetic properties of these systems. $LaFe_{0.5}Cr_{0.5}O_3$ exhibits a perovskite structure in which Fe^{3+} and Cr^{3+} are randomly distributed on the *B*-site and as indicated in the table their spins order AFM with a Néel temperature T_N of 265 K [35]. However, ferrimagnetism with a large saturation magnetization was reported below 50 K in thin films of $LaFe_{0.5}Cr_{0.5}O_3$ with ordered Fe/Cr cations [38]. Concerning *A*-site doping, the replacement of La by Bi has been considered in $LaFeO_3$ [39] and $LaCrO_3$ [40], and found to weaken the antiferromagnetic order of the undoped compounds (see Table 1). There are few investigations of Bi-doped LFCO with different concentrations of Fe and Cr [41-45]. These studies suggest a complex magnetic behavior, possibly related to the different type of interactions between the magnetic Fe/Cr cations.

In the current work $La_{0.75}Bi_{0.25}Fe_{1-x}Cr_xO_3$ (LBFCO; x = 0.1, 0.25, 0.5, and 0.75) polycrystalline samples are prepared and X-ray powder diffraction (XRPD), neutron powder diffraction (NPD), magnetic measurements, and other complimentary techniques have been employed to explore the structure and magnetic ordering of LBFCO. The effect of Cr substitution on the main orthorhombic perovskite distortion parameters in LBFCO is studied in detail.

2. Experimental procedure

2.1. Sample preparation

Ceramic samples of $La_{0.75}Bi_{0.25}Fe_{1-x}Cr_xO_3$ (x = 0.1, 0.25, 0.5, and 0.75) were synthesized by a standard ceramic technique from La_2O_3, Bi_2O_3, Fe_2O_3, and Cr_2O_3 (≥ 99.9% in purity) at ambient atmosphere using a programmable furnace. The method involved preparation of a powder-like mixture of initial reagents, pressing of this mixture under 3000 kg/cm^2, and sintering of the specimens in air at temperatures 950, 1000, and 1050^{o}C successively with several intermediate grindings. The series of grinding and sintering procedures were performed until the XRPD patterns showed the expected spectra without impurity phases. The overall duration of the sintering was approximately 36 h. After the final annealing, the specimens were cooled inside the furnace. The mixtures were weighed before and after heat treatment to determine possible Bi loss due to evaporation. In all cases, the weight difference was negligible (< 0.01%). For some concentrations (x = 0.1 and x = 0.25), the parasitic phases were leached out in 10% diluted HNO_3.

2.2. X-ray powder diffraction

The purity of the samples was checked from XRPD patterns obtained on a D-5000 diffractometer using Cu K_α radiation. The ceramic samples of LBFCO were crushed into powder in an agate mortar and suspended in ethanol. A Si substrate was covered with several drops of the resulting suspension, leaving randomly oriented crystallites after drying. The XRPD data for Rietveld analysis was separately collected at room temperature on a Bruker D8 Advance diffractometer (Ge monochromatised Cu $K_{\alpha1}$ radiation, Bragg-Brentano geometry, DIFFRACT plus software) in the 2θ range 10-152° with a step size of 0.02° (counting time was 20 s per step). The slit system was selected to ensure that the X-ray beam was completely within the sample for all 2θ angles. The samples were rotated to increase

powder averaging statistics. The diffraction patterns were analyzed with the Rietveld full-profile fitting approach from the FULLPROF program [46]. Pseudo-Voigt profile function was used for the fit of the peaks. A peak asymmetry correction was made for angles below 35° (2θ).

2.3. Chemical composition

The chemical composition of the prepared ceramic LBFCO samples was analyzed by energy dispersive spectroscopy (EDS) using a JEOL 840A scanning electron microscope and INCA 4.07 (Oxford Instruments) software.

2.4. Second harmonic generation (SHG) measurements

The materials were characterized by SHG measurements in reflection geometry, using a pulsed Nd:YAG laser (λ= 1.064μm). The SHG signal $I_{2\omega}$ was measured from the polycrystalline samples relative to α-quartz standard at room temperature in the Q-switching mode with a repetition rate of 4 Hz. To make relevant comparisons, the LBFCO microcrystalline powders and α-quartz standard were sieved into the same particle size range because it has been shown that the SHG efficiency strongly depends on particle size [47].

2.5. Magnetic measurements

The magnetization measurements were performed using a superconducting quantum interference device (SQUID) magnetometer from Quantum Design Inc. The temperature dependence of the magnetization was recorded in magnetic fields of H = 0.05 T and 0.5 T using zero-field-cooled (ZFC) and field-cooled (FC) measurement protocols. Magnetic hysteresis loops were recorded at low temperatures (T = 5 K).

2.6. Neutron powder diffraction

Due to significantly different neutron scattering length of iron and chromium (b_{Fe} = 9.45 fm, b_{Cr} =3.64 fm) [48], the neutron diffraction technique is an appropriate tool to analyse the occupation order on the *B*-site of the studied perovskites. This is not true for the *A*-sublattice where the difference between the neutron coherent scattering lengths for La and Bi is approximately 3% (b_{La} = 8.24, b_{Bi}= 8.53 fm) [48]. The neutron scattering length of oxygen (b_O = 5.805 fm) is comparable to those of the heavy atoms and NPD provides accurate information on its position and stoichiometry. Neutron diffraction patterns at various temperatures from 4 to 900 K were collected on the NPD instrument MEREDIT@NPI (Nuclear Physics Institute of the CAS, Czech Republic) using a neutron wavelength of 1.46 Å. Powder samples in vanadium containers were placed inside a closed cycle cryostat and a vacuum furnace for measurements from 4 K to room temperature and from room temperature to 900K, respectively. In all cases data were collected in an angular range from 4 to 144° 2θ with step of 0.08° 2θ. An instrument resolution function (IRF) describing the reflection shape given by the instrument obtained from pattern fitting of a SiO_2 standard using the same monochromator setting was used for the refinement. The diffraction patterns were analyzed with the Rietveld full-profile fitting approach from the FULLPROF program [46]. The diffraction peaks were described by Thompson-Cox-Hastings pseudo-Voigt profile function. A peak asymmetry correction was made for angles below 65° (2θ). Background intensities were estimated by interpolating between up to 40 selected points (low temperature NPD experimental data) or described by a polynomial with six refinable coefficients. The refined atomic coordinates were used to calculate the magnitude of the tilting angles and bond distances [49]. The IVTON software [50] was employed to characterize the coordination spheres of the A and *B*-site cations and to obtain bond lengths, volumes of coordination polyhedral and displacements of cations from the centers of the coordination polyhedra.

Earlier Mössbauer spectroscopy studied provided strong support for the existence of Fe and Cr solely in the trivalent state [51,52]; the magnetic structure was hence refined as an independent phase in which only Fe^{3+}/ Cr^{3+} cations were included. The magnetic propagation vector was determined from the peak positions of the magnetic diffraction reflections. Representational analysis to determine the symmetry allowed magnetic structures was performed using the programs BASIREPS [53]. Using the structural information extracted from NPD patterns, a symmetry-mode analysis of distorted LBFCO structures of displacive type was performed, and amplitudes and polarization vectors of the distortion modes of different symmetry frozen in the structure were calculated. Group-theoretical calculations were done using Bilbao Crystallographic Server software (AMPLIMODES: Symmetry mode analysis [54] and Magnetic Symmetry and Applications [55]).

3. Results

3.1. Sample characterization

The set of EDS analyses performed on several particles of each LBFCO sample shows the presence of all included cations with the concentration ratios of La/Bi and Fe/Cr equal to the stoichiometric ones within the limits of the experimental errors. The oxygen content, determined via iodometric titration, was between 2.97(2) and 3.02(2) for the different samples. All these values are quite close to the expected ratios and permit us to conclude that the composition of the samples is practically equal to the nominal values. The phase purity of the samples was ascertained using XRPD. Scanning electron micrographs showed that the average crystallite size decreases with increasing Cr concentration from 4.3 μm for x = 0.1 to 1.8 μm for x = 0.75. The SHG technique was used to ascertain the presence/absence of the centre of symmetry in the prepared ceramics. These measurements at room temperature gave a negative result for all samples suggesting that the investigated LBFCO samples are centrosymmetric.

However, after careful inspection of the NPD patterns, it was found that all powder samples prepared for NPD studies were composites of two phases with small amounts (2-4 vol.%) of Fe_2O_3. As mentioned above, the presence of Fe_2O_3 was not registered on the XRPD patterns. This may be due to the fact that for the NPD studies, several additional batches of the compounds were prepared and mixed together to increase the sample volume, and not all of the batches were checked by XRPD. The formation of Fe_2O_3 has been reported in many other studies [56-58] and has usually been attributed to the loss of a small amount of Bi_2O_3 from the stoichiometric mixtures during sample preparation. However, the presence of the Fe_2O_3 phase is not affecting the structural refinement of the main phase.

3.2. X-ray powder diffraction

All X-ray diffraction patterns at room temperature can be indexed using space group *Pnma* and show that the samples are free from impurities. Observed and calculated patterns are shown in Figure 1, and the results of the refinements, as well selected interatomic distances and angles are collected in the Supplemental Materials, Tables S1 and S2. Qualitatively, the overall XRPD patterns of the LBFCO samples are similar, in agreement with their common space group and low X-ray contrast for the ratio of Fe to Cr. Small shifts in reflection positions are due to changes of the orthorhombic distortion and the cell parameters with change in the Cr concentration. The lattice parameter of each axis gradually decreases with increasing Cr concentration (see Table S1), which is mainly due to the smaller size of Cr^{3+} compared to Fe^{3+}(the ionic radii of Cr^{3+} and Fe^{3+} are 0.615 Å and 0.645 Å, respectively [59]). The oxygen atoms in LBFCO occupy two distinct crystallographic positions, namely O1 (*4c*) and O2 (*8d*). The O1 atoms make two apices of the octahedra along the [0 1 0] direction,

while the remaining four apices in the plane perpendicular to the [0 1 0] direction are occupied by the O2 atoms. The Fe/CrO_6 octahedra are not rigid (deformed) and form three slightly different Fe/Cr–O bond lengths. The lengths of the metal-oxygen bonds (Fe/Cr-O1) are, for all samples in-between the lengths of the longer and the shorter of the (Fe/Cr-O2) bonds. This geometry is not common in Fe-based orthorhombic perovskites [1] since Fe^{3+} cations prefer a regular octahedral environment. Overall, the Fe/CrO_6 octahedral deformation increases with increasing chromium content. The bond angles Fe/Cr –O1– Fe/Cr and Fe/Cr – O2– Fe/Cr show irregular trends with increasing Cr content (Table S2).

The possibility of long range order of the Fe/Cr ions has been investigated in detail. No reflections associated with the ordering of the Fe^{3+} and Cr^{3+} cations (e.g. considering a small monoclinic distortion) were observed. Notably, the diffraction peaks in the XRPD patterns became broader with Cr substitution. This broadening could be caused by the observed reduction of the grain size, but also to some degree from increased fluctuations of the Fe/Cr occupancy between grains. With increasing x, the Goldschmidt tolerance factor *(t)* [60] increases slightly from 0.957 to 0.967, indicating that the substitution of Fe^{3+} by Cr^{3+} at the *B*-site could result in a reduction of the lattice distortion. These changes of the lattice metrics are connected with the influence of substitution on the *B*-sublattice only, in spite of the fact that the radius of Bi^{3+} (1.17 Å) is slightly larger than that of La^{3+} (1.16 Å) for coordination number 8, since the concentration of La and Bi is kept the same for all samples. The ratio $(a-c)/(a+c)$, which is independent of the oxygen coordinates, can also be used as a measure of octahedral distortions in an orthorhombic cell. This ratio, calculated using the room temperature XRPD results (Table S1), decreases with increasing Cr substitution.

The room temperature crystal structure of several compositions of LBFCO has previously been investigated using XRPD [41-45]. The lattice parameters here obtained for LBFCO are in reasonable agreement with those previously reported. Variation in the observed structural parameters is presumably attributed to differences in sample preparation conditions that may induce variations in the stoichiometry.

3.3. Magnetization

Due to the different magnetic moments of Fe^{3+} and Cr^{3+} and the random distribution of these ions on the *B*-site, the samples may behave as disordered antiferromagnets where the sublattices do not compensate each other perfectly, giving rise to a weak excess magnetic moment, as observed in $LaFe_{0.5}Cr_{0.5}O_3$ [35] and related compounds [41,45]. This moment and a possible weak ferrimagnetic moment from minute amounts of the Fe_2O_3 phase strongly influence the measured magnetization vs. temperature curves in ZFC and FC protocols. As a representative example, we show in Figure 2, *M* vs *T* curves (ZFC and FC) of $La_{0.75}Bi_{0.25}Fe_{0.5}Cr_{0.5}O_3$ recorded under a lower 0.05 T (upper panel), and a higher 0.5 T (lower panel) applied field. In the inset, an *M* vs. *H* curve on the same sample measured at 5 K is shown (see Supplemental Materials, Figure S1, for the corresponding data for $La_{0.75}Bi_{0.25}Fe_{0.25}Cr_{0.75}O_3$ for comparison). This curve shows that there is a weak spontaneous moment (of the order of 0.01 μ_B/f.u.) that is forced to align with the applied field at high fields well above the coercive field ($H_c \sim 1$ T). It is also seen from the figure that the paramagnetic response from the antiferromagnetic main phase causes a linear increase of the measured magnetic moment that is superposed on the contribution from the aligning of the spontaneous excess moment. The excess moment (its temperature dependent coercivity and temperature dependent magnitude (following the sublattice magnetization)) provides the dominating temperature dependent contribution to the measured *M* vs *T* curves in the main panel. One conclusion that can be drawn from the *M* vs *T* curves in the lower panel is that the coercivity of the excess moment has decreased to the order of 0.5 T at approximately 200 K. Otherwise, these curves reflect a complex interplay [41,45] between the spontaneous excess moment and

the susceptibility of the main phase and the contribution from the minute ferrimagnetic secondary phase. The Néel temperature of most of the LBFCO compositions was beyond the measurable range of our SQUID set up.
This complexity prompted us to perform detailed temperature dependent neutron diffraction studies on these samples to gain better insight into their magnetic properties. It is worth mentioning that our magnetization measurements were limited to 400 K, while the neutron diffraction patterns were recorded up to 900 K. This turned out to be significant because (as we show in the next section), the magnetic ordering temperature of most of these samples lie in the range 300 to 700 K.

3.4. Neutron powder diffraction

The crystal structure of the LBFCO samples was independently determined using NPD data measured above the magnetic ordering temperatures. Rietveld refinements were carried out in all possible centrosymmetric space groups, but a clearly superior fit was obtained for s. g. *Pnma* within the structural model derived from the XRPD study. This model describes a random distribution of Fe and Cr at the *B*-site. The distribution of the La and Bi cations at the *A*-site was found to be fully disordered as well (see Table 2). *A* and *B* sublattice occupancies were refined independently, after fixing the occupancies of one of the sublattice to those suggested by the EDS ratios. Ultimately, the oxygen occupancy was refined to a value close to 1.00 (in the frame of 2 standard deviations). No extra peaks or additional splitting of the main reflections that would indicate the need for symmetry lower than orthorhombic, were observed. After the final refinements, reasonable reliability factors were obtained. These values are included in Table 2 together with the final unit cell and atomic parameters.
The *Pnma* structure (see Figure 3(a)) was conserved over the studied temperature range (4-900 K) for all samples. The temperature evolution of the lattice parameters for different Fe/Cr content is shown in Figure 4; the corresponding evolution of the cell volume *V* is shown in Figure S2. The lattice parameters and cell volumes exhibited a near linear decrease with Cr content; the non-linearity possibly arising due to a varying temperature dependence of the magnetostrictive effects in-between compositions because of the decrease of T_N with increasing Cr concentration. The decrease of the cell volume with increasing x, in agreement with the size ratio between $Cr^{3+}$and Fe^{3+}cations, was also confirmed by the NPD results.
The employed structural model considered the bismuth and lanthanum ions to be equivalent at the *A*-site. This can be motivated since Bi^{3+} and La^{3+} have similar ionic radii, however, the effect of the Bi^{3+} lone pair electron has not been considered. Thus, the relative displacements of Bi^{3+} and La^{3+} away from the 'averaged' *A*-site position could be different. However, for structural analyses of the investigated compositions this is not critical because all samples have the same La/Bi ratio.
The evolution of the orthorhombic distortion $(a-c)/(a+c)$ of LBFCO with temperature and x is plotted in Figure 5. The evolution is not monotonous with temperature and shows non-linear trends with increasing Cr content. For comparison, the degree of the orthorhombic distortion of $LaFeO_3$ decreases with increasing temperature, whereas it increases in $LaCrO_3$ [61,62].
The orthorhombic crystal structure of LBFCO in polyhedral representation is shown in Figure 3(a). All the obtained distances are in good agreement with the values expected from the ionic radii sums for La^{3+}/Bi^{3+} cations (coordination number 9) and Fe^{3+}/Cr^{3+} cations (coordination number 6). Bond valence calculations on both *A*- and *B*-sites show very good agreement with the expected oxidation state of the ions – La^{3+}/Bi^{3+} and Fe^{3+}/Cr^{3+}. The observed, calculated, and difference neutron diffraction patterns of LBFCO sample with x = 0.1 at different temperatures are shown in Figure 6, as a representative example.
The structural parameters refined at 4, 295, and 900K are summarized in Table 2. The Fe/Cr octahedra are not rigid and, for all concentrations axially expanded. The two Fe/Cr-O2

distances are not equal, and change with the temperature and Cr concentration (see Figure 7). The O-Fe/Cr-O and Fe/Cr−O−Fe/Cr angles that can be regarded as measures of the distortion of the octahedra, are plotted in Figure 8 and Figure S3 as a function of temperature and Cr-concentration. In general, these angles increase with the temperature. Non-linear trends with Cr-concentrations are also quite evident. These changes in the Fe/Cr−O−Fe/Cr angles are influenced by changes in the degree of octahedral tilting as well as the distortion of the octahedra. The distortion is described by two possible tilting modes, the "in-phase" (tilting in the same sense around [010]) and "out-of-phase" (tilting in opposite sense around [101]) tilts [66]. Following [49], the tilt angles were calculated from the refined atomic coordinates extracted from the NPD patterns at different temperatures. It was found that the in-phase tilts are smaller in comparison with the out-of-phase tilts for all concentrations of Cr. These tilt angles decrease progressively as the temperature is increased (see Figure 9), showing that the structure becomes less distorted at higher temperatures. The in-phase tilts vary in a quite smooth manner over the entire temperature range. However, for several concentrations and temperature intervals the out-of-phase tilts show sharp discontinuities indicating sudden minor structural transformations. For example, for x = 0.1, the Fe/Cr-O1-Fe/Cr and Fe/Cr−O2−Fe/Cr angles display an abrupt increase and decrease, respectively, around 450K. The Fe/Cr−O1−Fe/Cr angle is influenced by the out-of-phase tilt whereas the Fe/Cr−O2−Fe/Cr angle is influenced by both tilts. An increasing Fe/Cr−O−Fe/Cr angle suggests a decreasing octahedral tilt, neglecting minor octahedral distortion effects. The increase of the Fe/Cr−O1−Fe/Cr angle suggests a decrease in the out-of-phase tilt, while the decrease of the Fe/Cr−O2−Fe/Cr angle suggests an increase in the in-phase tilt. A combination of octahedral and unit cell distortion is necessary to accommodate the size mismatch between La/Bi and Fe/Cr, but the relative contributions can vary with temperature and degree of chemical pressure related with Cr substitution. The expansion of the unit cell axes with temperature is clearly influenced by the thermal evolution of both the Fe/Cr–O bond lengths and inter-octahedral (Fe/Cr–O–Fe/Cr) and intra-octahedral (O–Fe/Cr–O) bond angles. It is important to note that the Fe/Cr–O1 bond has its largest component along the *b*-axis, and the expansion of this bond is mainly responsible for the change of the *b*-axis. In contrast, the Fe/Cr–O2 bond lengths are primarily responsible for the changes in the *a*- and *c*-axes.

The La/Bi cations are effectively 9-coordinated and displaced in the *xz*-plane in the *Pnma* structure. With increasing temperature, the displacement of La/Bi from its high-symmetry position decreases monotonically with the temperature. The larger displacement along the *x*-axis is more sensitive to temperature than the smaller displacement along the ***z***-axis, the latter showing only a subtle variation with increasing temperature. With increasing Cr substitution, the displacement of La/Bi along the *x*-axis decreases monotonically. Any displacement along the *z*-axis is not evident.

The polyhedral volume of the A-site dodecahedron (V_A) and B-site octahedron (V_B) increases monotonically with temperature without discernible discontinuity (see Table 3). A volume contraction of both (V_A) and (V_B) is observed with increasing Cr doping. The size mismatch between the AO_{12} and BO_6 polyhedra in the perovskite structure (V_A/V_B) is equal to 5.0 in the absence of octahedral tilting (c.n. = 12) and decreases with increasing octahedral tilting [67]. V_A/V_B increases monotonically with temperature for all Cr concentrations.

For the high-temperature NPD patterns of x = 0.75, a broadening of reflections was evident and the Rietveld analysis was quite complicated owing to the large variations of the refined parameters depending on the model used (with and without anisotropic broadening). The best fits were obtained for the model with two perovskite phases with the same symmetry. The atomic positions and isotropic temperature factors were constrained to be the same for the two phases while lattice parameters and phase fractions were allowed to vary independently. The

fit was improved but the output had larger uncertainties in the refined parameters and strong correlation between the refined fractions. For unambiguous interpretation of the broadened reflections in LBFCO with x = 0.75, detailed high-resolution electron microscopy and electron diffraction studies are required. Magnetostriction that leads to a highly unusual structural response [68] is allowed by symmetry in LBFCO. Possible magnetoelastic coupling can cause the structural non-linearity and unexpected features observed for several investigated compounds (x = 0.1, 0.25, and 0.5).

3.5. Mode crystallography

Mode crystallographic analysis was performed using the AMPLIMODES suite at Bilbao Crystallographic Server [54,55], and the Rietveld refined coordinates from the NPD patterns. The program AMPLIMODES calculates the amplitude of symmetry-adapted modes for the low symmetry distorted structure (*Pnma*) with respect to a high symmetry structure. These modes are given in relative units using atomic displacements of the atoms in the asymmetric unit of the distorted phase. The analysis using AMPLIMODE requires the parent (or high symmetry (HS)) structure, the low symmetry structure (LS) and the transformation matrix for the two phases, and the symmetry adapted primary and secondary modes that transform the HS phase into the LS phase. In our analysis, we have considered the hypothetical cubic space group *Pm*-3*m* as HS phase, with a lattice parameter estimated from the NPD data at 900 K as $a = V^{1/3}/8$. As illustrated in Figure 10, a single distortion component is not sufficient to describe the symmetry break of the transformation from the cubic to the orthorhombic phase i.e, the *Pnma* phase cannot be generated by a single mode distortion. Seven modes are required to arrive at the *Pnma* structure from the *Pm-3m* structure: octahedral tilting modes, *R4+* (out-of-phase tilt) and *M3+* (in-phase tilt), octahedral distortion modes, *X5+*, *R5+* and *M2+*, and *A*-site cation displacement modes, *R5+* and *X5+*. It was found that the displacive phase transition *Pm-3m*→*Pnma* requires splitting of the cubic Wyckoff sites through these vibrational modes in the following manner:

(i) La/Bi at the 1b site of *Pm-3m* goes to the *4c* site via *R5+(1)* and *X5+(1)* modes,

(ii) O at 3d site goes to O1 at 8d and O2 at *4c* via *R4+(1), R5+(1), X5+(1), M2+(1)* and *M3+(1)* modes,

(iii) Fe/Cr at the 1a site remains at its original position.

More specifically, the *R4+* distortion corresponds to the tilt of octahedra around the *a* direction (out-of-phase octahedral tilting). *M3+* corresponds to the tilt of octahedra around the *b* direction. The modes *X5+* and *R5+* involve both oxygen and La/Bi cation displacements. *X5+* implies displacement of the apical O atoms along the *b* axis and alternating displacements of the La/Bi atoms along *a* direction. *R5+* mainly involves alternating displacements of La/Bi atoms along the *c* direction. The amplitude of the *M2+* mode represents the displacement of the O atoms in the square equatorial planes of the octahedra to transform them into a rhombus. One can see in Table 5 that for all Cr contents the *Pnma* distortion in LBFCO is similar. The structure is composed mainly by two modes with symmetries labeled *R5+* and *M2+* as indicated by the much larger amplitudes of these two modes and the fact that they can explain the symmetry break into the *Pnma* space group, in agreement with the structural results (cation displacements and bond angles). On the other hand, although the rest of the modes are secondary ones, they make noticeable contributions to the final structural model. The amplitude of the dominating *R5+* and *M2+* modes slightly decrease as the Cr content increases. The amplitude of the *M3+* mode is around 0 within the experimental resolution.

3.6. Magnetic structure determination

An additional increase of several Bragg reflections, expected for an antiferromagnetic state below T_N are clearly visible in Figures 11 and 12, indicating that a long-range magnetically ordered state is achieved. Moreover, the intensity of these peaks decreases as the temperature increases and becomes negligible above a definite temperature, confirming them to be magnetic in origin since the nuclear structure is the same at all temperatures. In the neutron diffraction patterns collected at 4 K, several Bragg reflections corresponding to the *Pnma* structure, notably (011), (112/211/031), and (013/132), exhibited a significant increase in intensity compared to the patterns measured at high temperatures. This increase can be attributed to the magnetic ordering. The fact that the positions of these magnetic intensities are superposed on the nuclear structure Bragg positions leads to the propagation vector of the magnetic structure k = (0, 0, 0). In other words, the nuclear and magnetic structures have the same unit cell. To find possible magnetic arrangements of the *B*-site (4b) spins, irreducible representation analysis using BASIREPS software [53] was performed. There are four possible spin arrangements $\Gamma 1$, $\Gamma 3$, $\Gamma 5$, and $\Gamma 7$ (see Table 4). In all representations, the spins can have components along all three axes. $\Gamma 3$, $\Gamma 5$ and $\Gamma 7$ have one ferromagnetic component along a different axis. Only $\Gamma 1$ has antiferromagnetic arrangement in all three directions. By testing all the proposed models we concluded that the best fits of the neutron diffraction patterns can be obtained using the $\Gamma 1$ irreducible representation with a single component along the *x*-axis. Contributions along the *y*- and *z*-axes were negligible and were fixed to zero in the refinements. Using the magnetic space group notion the magnetic structure is *Pnma* (62.441). The total magnetic moment of the unit cell is zero in the ideal AFM structure illustrated in Figure 3(b). The variation of the refined magnetic moments with the temperature is plotted in Figure 13 for the different LBFCO compositions. The most important features of the magnetic structure refinement are reported in Table 2 and the good agreement between the observed and calculated NPD patterns at T = 4 K is shown in Figure 6 for the sample with x = 0.1. The magnetic moments on the Fe/Cr atoms decrease with temperature (see Figure 13) and allow the determination of T_N as: 700, 500, 350, and 300 K for x = 0.1, 0.25, 0.5 and 0.75, respectively. Diffuse intensities of the magnetic reflections above these temperatures (see Figures 11 and 12) may reflect a possible short-range order of magnetic cations in the *B*-sublattice of LBFCO.

The magnetic arrangement is that of a *G*-type antiferromagnet with an antiparallel coupling of the Fe^{3+}/Cr^{3+} cations to their six nearest neighbors, all spins being aligned along the *a*-direction. The magnitude of the magnetic moment at 4 K of the Fe^{3+}/Cr^{3+} cations for all investigated samples was found to be lower than the calculated values for the individual Fe/Cr ratio (5.0 μ_B/Fe and 3.0 μ_B/Cr). The structural disorder may be partly responsible for the lower values of the ordered magnetic moments observed in the samples.

4. Discussion

All investigated LBFCO samples were found to order in a disordered antiferromagnetic structure. The disorder is caused by random distribution of the Fe and Cr cations at the *B*-site. The disordered structure implies that there is an excess spontaneous magnetic moment that aligns with an applied magnetic field and dominates the magnetic response from the main phase at low applied magnetic fields. As discussed above, this makes the interpretation of the macroscopic magnetization experiments difficult and often leaves too much room to speculation. On the other hand, the results from the NPD experiments evidence antiferromagnetic *Gx*-type ordering in all samples with a Néel temperature that decreases with increasing Cr content.

In the *Pnma* crystal structure, the *B*-site (Fe/Cr) lies on an inversion center and there are three independent Fe/Cr–O bond lengths, three independent O–Fe/Cr–O bond angles, and two

independent Fe/Cr– O–Fe/Cr bond angles for the two unique O sites. In the symmetry-mode approach, the seven independent positional parameters of the *Pnma* structure can be described as seven internal modes [70]: two octahedral 'tilts', three octahedral distortions, and two A-site cation displacements. The concentration and temperature dependence of these distortion parameters are derived from XRPD and NPD experiments and are described, reviewed, and plotted in the text, tables, and figures of the results section. Certain features are especially compelling:

For octahedral tilting distortion alone (tilt system $a^-b^+a^-$), the lattice metrics $a > b/\sqrt{2} > c$ is expected. This relationship holds for the entire $LnFeO_3$ series [61,71,72], that is consistent with the fact that octahedral tilting is essentially the only distortion mechanism present in that series. For the samples with low Cr concentration (x = 0.1 and 0.25), $a > c > b/\sqrt{2}$ is obeyed at all temperatures. This is in contrast with the situation for x = 0.5, where the NPD data indicate $c > a > b/\sqrt{2}$ and for x = 0.75 where $c > b/\sqrt{2} > a$. The case with $c > a$ is unusual but also occurs in pure $LaCrO_3$ [62,73]. The room temperature XRPD results indicate a similar trend, but do not confirm the sign shift of $(a-c)/(a+c)$ at higher concentrations of Cr. This can be explained by the fact that the distortions are small (near the resolution limit of the analysis) and the samples for NPD and XRPD are taken from different preparation batches.

Changes in the *c*-lattice parameter reflect the magnitude of the octahedral tilting distortion [73], whereas changes in the *a*-lattice parameter can serve as an indicator of the magnitude of cooperative Jahn-Teller distortions. It is, however, known [74, 75] that the combination of octahedral tilting and a cooperative Jahn-Teller distortion (orbital ordering) can produce yet another combination of lattice metrics: $a > c > b/\sqrt{2}$. In this context, it is worth mentioning that the temperature dependence of the lattice constant *a* in the sample with x = 0.75 is anomalous and shows negative thermal expansion coefficient in the temperature range 400-800 K. Such an anomalous behavior is not observed for the samples with x = 0.1, 0.25, and 0.5.

To gain further understanding of the structural data for the LBFCO samples, the IVTON software [50] was employed to perform a polyhedral analysis of the structure and characterize the coordination spheres of the *A* and *B* cations, and to obtain bond lengths and displacements of the cations from the centers of the coordination polyhedra. The obtained results are given in Table 3. The first observation is that the *A*-site cations have shifted significantly (approximately 0.22 Å for all samples and temperatures) away from the center of its coordination polyhedron. The *B*-site cations have not moved away from the octahedral centers. The changes of the average bond distances A-O and B-O are marginal, but overall follow the decreasing trend set by the smaller size of the Cr^{3+} compared to Fe^{3+}.

Octahedral tilting in orthorhombic perovskites results in a reduction of the lattice parameters perpendicular to the tilt axis saving the parameter parallel to this axis unchanged. Therefore, the tilting angles can be roughly estimated using the related unit cell metrics. For LBFCO the observed variation of the lattice parameters indicates that the tilting decreases with increasing Cr content. The tilting results in reduction of the coordination number (c.n.) of an *A*-site cation (12 in the undistorted cubic structure). In most orthorhombic perovskites, c.n. may vary between 8 and 12, depending on the tilt angle and ratio between the sizes of *A*- and *B*-site cations. For LBFCO the value of the *A*-site coordination number is practically the same (c.n. = 9) for different values of x.

The structure of LBFCO is characterized by several different '180° Fe/Cr-O-Fe/Cr bonds' (see Figure 8). The magnetic structure can be explained from AFM superexchange interactions along the Fe/Cr-O chains where the Fe/Cr-Fe/Cr distance is approximately 3.9 Å. Changes in bond distances and bond angles are known to influence both the sign and strength of the superexchange interaction. It was found that the Fe/Cr-O-Fe/Cr angles decrease with increasing concentration of Cr. However, the decrease of T_N with increasing Cr content is well

described by the linear trend set by the end members x = 0.1 (T_N = 700 K) and x = 0.75 (T_N = 300 K), of this study.

Before being able to draw solid conclusions about the origin of the structural distortions, one should explore the oxidation and spin states of Fe and Cr further. If the oxidation states of Fe and Cr differ from the above assumed ones, the average ionic radii at the *B* site and variation in the tolerance factor may be different with Cr doping. Additional Mössbauer and X-ray absorption spectroscopies, that can explore the oxidation state and the local structure around the probing atom, can be extremely useful in future investigations.

5. Conclusions

In summary, we have successfully synthesized powder samples of $La_{0.75}Bi_{0.25}Fe_{1-x}Cr_xO_3$ (x = 0.1, 0.25, 0.5, and 0.75) solid solutions using a solid state reaction route. XRPD and NPD data suggest that there was no long-range order of *B*-site ions in the samples. At all temperatures and Cr doping levels, the crystal structure was orthorhombic with space group *Pnma*. The orthorhombic phase was described using crystallographic distortion mode analysis and polyhedral analysis. The temperature and Cr concentration dependence of the lattice parameters and associated orthorhombic distortion, Fe/Cr-O bond lengths and Fe/Cr-O-Fe/Cr bond angles was investigated in detail. Changes in the octahedral tilt system with Cr doping were observed, as well as the decrease of the Fe/Cr-O-Fe/Cr bond angles.

The magnetic and structural properties of LBFCO compounds are considerably more complex than the prototypical end members. However using NPD the onset of antiferromagnetic ordering, as well as the magnetic structure (*Gx*-type ordering) of the compounds could be determined. The onset of magnetic ordering was found to decreases with increasing Cr content, from approximately 700 K (x = 0.1) to 300 K (x = 0.75).

Acknowledgements

Financial support from the Swedish Research Council (VR), the Swedish Foundation for International Cooperation in Research and Higher Education (STINT) and the Russian Foundation for Basic Research is gratefully acknowledged.

References

[1] R. H. Mitchell, Perovskites: Modern and Ancient, Almaz Press, Thunder Bay, 2002.
[2] N. A. Spaldin, Topics Appl. Physics 105 (2007) 175-218.
[3] J. F. Scott, Nature Mater. 6 (2007) 256-257.
[4] N.A. Spaldin, S.W. Cheong, R. Ramesh, Phys. Today 63-10 (2010) 38-43.
[5] Y. Tokura, S. Seki, Adv. Materials 22 (2010), 1554-1565.
[6] X. Yang, Z. Zhou, T. Nan, Y. Gao, G. M. Yang, M. Liu, N. X. Sun J. Mater. Chem. C 4 (2016) 234-243.
[7] K. F. Wang, J. M. Liu, Z. F. Ren, Adv. Phys. 58 (2009) 321–448.
[8] A. Roy, R. Gupta, A. Garg, Multiferroic Memories, Adv. Condens. Matter Phys., Hindawi Publ. Corp., New York, 2012 article 926290.
[9] R. Ramesh, N. A. Spaldin, Nature Mater. 6 (2007) 21-29.
[10] X. W. Qi, H. F. Wang, W. Q. Han, P. H. Wang-Yang, J. Zhou, Z. X. Yue Int. J. Modern Physics B 23 (2009) 3556-3560.
[11] C. N. R. Rao, A. Sundaresan, R. Saha J. Phys. Chem. Lett. 3 (2012) 2237-2246.
[12] J. F. Scott NPG Asia Materials 5 (2013) e72.

[13] R. Nechache, C. V. Cojocaru, C. Harnagea, C. Nauenheim, M. Nicklaus, A. Ruediger, F. Rosei, A. Pignolet, Adv. Mater. 23 (2011) 1724–1729.
[14] R. Nechache, C. Harnagea, A. Pignolet, J. Phys.: Condens. Matter 24 (2012) 096001.
[15] L. Sha, J. Miao, S. Z. Wua, X. G. Xu, Y. Jiang, L. J. Qiao J. Alloys Comp. 554 (2013) 299–303.
[16] S. Picozzi, C. Ederer, J. Phys.: Condens. Matter 21 (2009) 303201.
[17] P. Baettig, C. Ederer, N. A. Spaldin, Phys. Rev. B 72 (2005) 214105.
[18] M. N. Iliev, P. Padhan, A. Gupta, Phys. Rev. B 77 (2008) 172303.
[19] J. Wua, Z. Fan, D. Xiao, J. Zhu, J. Wang Prog. Mater. Sci. 84 (2016) 335–402.
[20] J. Sahu, C. R. Serrao, N. Ray, U. V. Waghmare, C. N. R. Rao, J. Mater. Chem. 17 (2007) 42-44.
[21] P. Mahadevan, N. Shanthi, D. D.Sarma, J. Phys.: Condens. Matter 9 (1997) 3129.
[22] Rajeswaran, D. I. Khomskii, A. K. Zvezdin, C. N. R. Rao, A. Sundaresan Phys. Rev. B 86 (2012) 214409.
[23] Y. Tokunaga, N. Furukawa, H. Sakai, Y. Taguchi, T. Arima, Y. Tokura, Nature Mater. 8 (2009) 558-562.
[24] J.-H. Lee, Y. K. Jeong, J. H. Park, M.-A. Oak, H. M. Jang, J. Y. Son, J. F. Scott, Phys. Rev. Lett. 107 (2011) 117201.
[25] W. Wang, M. O. Tadé, Z. Shao, Chem. Soc. Rev. 44 (2015) 5371-5408.
[26] S. Acharya, J. Mondal , S. Ghosh , S. K. Roy , P. K. Chakrabarti, Mater. Lett. 64 (2010) 415.
[27] M. Idrees, M. Nadeem, M. Atif, M. Siddique, M. Mehmood, M. M. Hassan, Acta Mater. 59 (2011) 1338-1345.
[28] M. Eibschutz, S. Shtrikman, D.Treves, Phys. Rev. 156 (1967) 562-577.
[29] S. A. Ivanov, R. Tellgren, F. Porcher, T. Ericsson, A. Mosunov, P. Beran, S. K. Korchagina, P. Anil Kumar, R. Mathieu, P. Nordblad, Mater. Res. Bull. 47 (2012) 3253-3268.
[30] S.C.Abrahams, R.L.Barns, R.L.Bernstein, Solid State Commun. 10 (1972) 379-381.
[31] A. Fossdal, M. A. Einarsrud, T. J. Grande, Europ. Ceram. Soc. 25 (2005) 927-933.
[32] K. Miura and K. Terakura, Phys. Rev. B 63 (2001) 104402.
[33] J. Kanamori, J. Phys. Chem. Solids 10 (1959) 87–98.
[34] J. B. Goodenough, Phys. Rev. 100 (1955) 564–573.
[35] A. K. Azad, A. Mellergard, S.-G. Eriksson, S. A. Ivanov, S. M. Yunus, F. Lindberg, G. Svensson, R. Mathieu, Mater. Res. Bull. 40 (2005) 1633-1644.
[36] R. Saha, A. Sundaresan, C. N. R. Rao, Mater. Horiz. 1 (2014) 20-31.
[37] L.Yuan, K. Huang, C. Hou, W. Feng, S. Wang, C. Zhou, S. Feng, New J. Chem. 38 (2014) 1168-1172.
[38] S. Chakraverty, A. Ohtomo, D. Okuyama, M. Saito, M. Okude, R. Kumai, T. Arima, Y. Tokura, S. Tsukimoto, Y. Ikuhara, M. Kawasaki, Phys. Rev. B 84 (2011) 064436.
[39] D. A. Rusakov, A. M. Abakumov, K. Yamaura, A. A. Belik, G. Van Tendeloo, E. Takayama-Muromachi, Chem. Mater. 23 (2011) 285–292.
[40]. H. -Y. Guo, J. I. L. Chen, Z. -G. Ye, A. S. Arrott, J. Mater. Res. 22 (2007) 2081-2086.
[41] K. Vijayanandhini, Ch. Simon, V. Pralong, Y. Breard, V. Caignaert, B. Raveau, P. Mandal, A. Sundaresan, C. N. R. Rao, J. Phys.: Condens. Matter 21 (2009) 486002.
[42] F. Bai, L. Shi, H. Zhang, Z. Zhong, W. Wang, D. He, J. Appl. Phys. 111 (2012) 07C702.
[43] J. K. Murthy, A. Venimadhav, Physica B 448 (2014) 162–166.
[44] B. Merabet, H. Alamri, M. Djermouni, A. Zaoui, S. Kacimi, A. Boukortt, M. Bejar Chin. Phys. Lett. 34 (2017) 016101.

[45] M. E. Villafuerte-Castrejon, M. García-Guaderrama, L. Fuentes, J. Prado-Gonjal, A. M. Gonzalez, M. A. de la Rubia, M. García-Hernandez, E. Moran, Inorg. Chem. 50 (2011) 8340–8347.
[46] J. Rodrıguez-Carvajal, Physica B 192 (1993) 55-69.
[47] S. K. Kurtz, T. T. Perry, J. Appl. Phys. 39 (1968) 3798-3812.
[48] V. F. Sears, *in* International Tables for Crystallography" (A. J. C. Wilson, Ed.), Vol. C, pp. 383-391. Kluwer Academic, Dordrecht, 1992.
[49] B. Kennedy, C. Howard, B. Chakoumakos, J. Phys.: Condens. Matter 11 (1999) 1479–1488.
[50] T. B. Zunic, I. Vickovic, J. Appl. Crystallogr. 29 (1996) 305-306.
[51] M. V. Kuznetsov, Q. A. Pankhurst, I. P. Parkin, Y. G. Morozov J. Mater. Chem., 11 (2001**)** 854-858.
[52] A. S. Sigov, V. S. Pokatilov, A. O. Makarova, V. V. Pokatilov Dokl. Phys. 59 (2014) 267-270.
[53] J. Rodriguez-Carvajal, BASIREPS: a program for calculating irreducible representations of space groups and basis functions for axial and polar vector properties, 2007.
[54] D. Orobengoa, C. Capillas, M. I. Aroyo, and J. M. Perez-Mato, J. Appl. Crystallogr. 42 (2009) 820-833.
[55] J. M. Perez-Mato, S. V. Gallego, E. S. Tasci, L. Elcoro, G. de la Flor, M. I. Aroyo, Annu. Rev. Mater. Res. 45 (2015) 217-248.
[56] C.M. Kavanagh, R. J. Goff, A. Daoud-Aladine, P. Lightfoot, F. D. Morrison, Chem. Mater. 24 (2012) 4563−4571.
[57] J.B. Li,_G. H. Rao, J. K. Liang, Y. H. Liu, J. Luo, J. R. Chen, Appl. Phys. Lett. 90 (2007) 162513.
[58] S. Singh, S. Kumar, R. Sandhu, M. Singh, A. Singh, IJEAR 5 (2015) 23-24.
[59] R. D. Shannon, Acta Crystallogr. A 32 (1976) 751–767.
[60] V. M. Goldschmidt, Naturwissenschaften 14 (1926) 477-485.
[61] C. A. L. Dixon, C. M. Kavanagh, K. S. Knight, W. Kockelmann, F. D. Morrison, P. Lightfoot, J. Solid State Chem. 230 (2015) 337–342.
[62] A. Martinelli, M. Ferretti, M. R. Cimberle, C. Ritter, Mater. Res. Bull. 46 (2011) 190–193.
[63] K. Momma, F. Izumi, "VESTA 3 for three-dimensional visualization of crystal, volumetric and morphology data", J. Appl. Crystallogr. 44 (2011) 1272-1276.
[64] K. Oikawa, T. Kamiyama, T. Hashimoto, Y. Shimojyo, Y. Morii, J. Solid State Chem. 154 (2000) 524-529.
[65] A. Shahee, D. Kumar, N. P. Lalla, AIP Conf. Proc. 1349 (2011) 1243-1244.
[66] D. Wang, R. J. Angel, Acta Cryst. B 67 (2011) 302–314.
[67] M. Avdeev, E.N. Caspi, S. Yakovlev, Acta Cryst. B 63 (2007) 363–372.
[68] A. C. Komarek, H. Roth, M. Cwik, W.-D. Stein, J. Baier, M. Kriener, F. Bourée, T. Lorenz, M. Braden, Phys. Rev. B 75 (2007) 224402.
[69] S. Ivantchev, E. Kroumova, G. Madariaga, J. M. Perez-Mato, M. I. Aroyo, J. Appl. Crystallogr. 33 (2000) 1190-1191.
[70] A. Gómez-Pérez, J. C. Pérez-Flores, C. Ritter, K. Boulahya, G. R. Castro, F. García-Alvarado , U. Amador, J. Appl. Cryst. 47 (2014) 745-754.
[71] J. -S. Zhou, J. B. Goodenough, Phys. Rev. Lett. 94 (2005) 065501.
[72] S. M. Selbach, J. R. Tolchard, A. Fossdal, T. Grande, J. Solid State Chem. 196 (2012) 249–254.
[73] J.-S. Zhou, J. A. Alonso, A. Munoz, M. T. Fernandez-Dıaz, J. B. Goodenough Phys. Rev. Lett. 106 (2011) 057201.

[74] P. M. Woodward, T. Vogt, D. E. Cox, A. Arulraj, C. N. R. Rao, P. Karen, A. K. Cheetham, Chem. Mater. 10 (1998) 3652-3665.
[75] T. Chakraborty, R. Yadav, S. Elizabeth, H. L. Bhat, Phys. Chem. Chem. Phys. 18 (2016) 5316-5323.

Figure captions

Figure 1. Rietveld refinement plot of the XRPD data collected on LBFCO samples with x = 0.1, 0.25, 0.5 and 0.75 at 295 K. The open circles are the observed data. The continuous line is the Rietveld refined pattern. The difference pattern is shown below as a solid line. The vertical bars are the peak markers.

Figure 2. Temperature evolution of the magnetization of $La_{0.75}Bi_{0.25}Fe_{0.5}Cr_{0.5}O_3$ recorded under magnetic fields of (a) 0.05 T, and (b) 0.5 T. The inset shows the isothermal magnetization curve at T = 5 K.

Figure 3. (a) Sketch of perovskite structure of LBFCO samples. (b) The antiferromagnetic *Gx*-type structure of the Fe/Cr sublattice of LBFCO below T_N. Structures drawn using VESTA[63].

Figure 4. Evolution of the cell edges between 4 and 900 K for the LBFCO samples. Error bars are smaller than the symbols. Solid lines are guides to the eye.

Figure 5. Temperature dependence of the orthorhombic distortion *(a-c)/(a+c)* calculated from the NPD data. The corresponding data calculated from lattice parameters from earlier NPD studies is added for comparison: $LaFeO_3$ (diamonds; tabulated data from [61]), $LaCrO_3$ (squares; data from [62] and [64]), $LaFe_{0.5}Cr_{0.5}O_3$ (triangles; from [35]). The effect of Bi substitution on the orthorhombic distortion is illustrated in the inset for Bi-doped $LaFeO_3$ [39] and $LaCrO_3$ [65] (calculated from XRPD data in both cases).

Figure 6. Final Rietveld plots after refinements of NPD patterns of LBFCO with x = 0.1 obtained at (a) 900 K, (b) 295 K, and (c) 4 K. The open circles are the observed data. The continuous line is the Rietveld refined pattern. The difference pattern is shown below as a solid line. Tick marks indicate reflections for LBFCO (upper marks; (a): nuclear reflections, (b, c): nuclear and magnetic reflections) and Fe_2O_3 (lower marks; nuclear and magnetic reflections).

Figure 7. Fe/Cr–O bond lengths as a function of temperature for LBFCO samples.

Figure 8. Temperature evolution of Fe/Cr-O-Fe/Cr bond angles.

Figure 9. Temperature dependence of in-phase and out-of-phase tilting angles for LBFCO perovskites.

Figure 10. Graph of maximal subgroups relating the space groups of the parent *Pm-3m* and *Pnma* phase of LBFCO. Figure obtained with SUBGROUPGRAPH [69].

Figure 11. Thermal evolution of NPD patterns for different LBFCO concentrations. Arrows indicated most intensive magnetic reflection**.**

Figure 12. Results of NPD study of LBFCO plotted as color maps**.**

Figure 13. Thermal and concentration evolution of magnetic moment at the Fe/Cr site for LBFCO compositions. Literature data for $LaFeO_3$ [61] and $LaCrO_3$ [62] is added for comparison.

Table 1. Comparison of antiferromagnetic transition temperature (T_N) and low temperature remanent magnetization M_r values extracted from *M* vs. *H* curves at low temperatures for related compounds from literature.

Compound	**T_N (K)**	**M_r in μ_B/f.u. (temperature)**	**Ref.**
$LaFeO_3$	760	~ 0.02 (10 K)	[29]
$LaCrO_3$	285	0 (10 K)	[40]
$LaFe_{0.5}Cr_{0.5}O_3$	265	0.04 (10 K)	[35]
	~ 50 (*film with cation ordering*)	1.5 (5 K)	[38]
$La_{0.75}Bi_{0.25}FeO_3$	Not reported	~ 0.02 (5 K)	[39]
$La_{0.7}Bi_{0.3}CrO_3$	230	0.02 (10 K)	[40]
$La_{1-y}Bi_yFe_{0.5}Cr_{0.5}O_3$ y ~ 0.25 to 0.5	Complex magnetic behavior	0.02 (4 K)	[45]
	Complex magnetic behavior	< 0.01 (5 K)	[41]

Table 2. Summary of structural refinement results of LBFCO samples using NPD data, s.g. *Pnma* [Wyckoff positions: La/Bi–*4c* (*x*,0.25,*z*), Fe/Cr- *4b* (0,0,0.5), O1−*4c* (*x*,0.25,*z*), and O2−*8d* (*x*,*y*,*z*)]. Error of measurement for lattice parameters was less than 0.0001 Å. Standard deviation of coordinates is less than 4 x 10^{-4} for cations and 6 x 10^{-4} for oxygen anions. Standard deviation of thermal parameters did not exceed 0.02 $Å^2$ for cations and 0.04 $Å^2$ for anions.

Phase (x)	**0.1**			**0.25**			**0.5**			**0.75**		
T, K	4	295	900	4	295	900	4	295	900	4	295	900
a, Å	5.5489	5.5568	5.5898	5.5380	5.5438	5.5760	5.5164	5.5258	5.5587	5.4854	5.4953	5.5111
b, Å	7.8335	7.8433	7.8935	7.8144	7.8274	7.8669	7.7907	7.7985	7.8423	7.7698	7.7754	7.8304
c, Å	5.5399	5.5457	5.5848	5.5332	5.5377	5.5751	5.5209	5.5266	5.5631	5.51	5.5170	5.5453

											09		
	La/Bi	0.763/0.236(5)			0.752/0.248(5)			0.744/0.256(5)			0.738/0.262(6)		
La/Bi	*x/a*	-0.0324	-0.0320	-0.0280	-0.0274	-0.0286	-0.0261	-0.0267	-0.0281	-0.0240	-0.0240	-0.0253	-0.0191
	z/c	0.0016	0.0023	0.0045	0.0122	0.0125	0.0101	0.0069	0.0075	0.0068	0.0054	0.0069	0.0059
	B (Å^2)	0.57	0.66	0.86	0.51	0.59	0.89	0.45	0.69	0.91	0.49	0.72	0.93
Fe/Cr	Fe/Cr	0.917/0.083(6)			0.764/0.236(6)			0.477/0.523(6)			0.236/0.764(7)		
	B(Å^2)	0.54	0.57	0.71	0.44	0.49	0.79	0.41	0.51	0.81	0.38	0.47	0.84
O1	*x/a*	0.5054	0.5058	0.5120	0.5097	0.5104	0.5091	0.5133	0.5070	0.5017	0.5084	0.5067	0.5105
	z/c	-0.1012	-0.0963	-0.0954	-0.0828	-0.0809	-0.0858	-0.0820	-0.0847	-0.0814	-0.08005	-0.0827	-0.0747
	B (Å^2)	0.33	0.45	0.87	0.41	0.58	0.93	0.45	0.67	1.02	0.48	0.71	1.15
O2	*x/a*	0.7226	0.7194	0.7234	0.7153	0.7170	0.72130	0.7159	0.7207	0.72550	0.73540	0.7265	0.7332
	y/b	0.0325	0.0317	0.0299	0.0350	0.0356	0.02930	0.0350	0.0326	0.03006	0.03038	0.0320	0.0332
	z/c	0.2848	0.2847	0.2837	0.2846	0.2859	0.28211	0.2803	0.2826	0.28201	0.28222	0.2818	0.2722
	B (Å^2)	0.44	0.51	1.13	0.53	0.64	1.243	0.56	0.74	1.28	0.59	0.78	1.26
Rp		3.68	3.55	3.34	3.48	3.17	3.40	3.76	3.54	3.29	3.37	4.16	

Rwp	4.69	4.53	4.26	4.42	3.96	624.475	4.32	4.51	4.50	4.24	4.29	5.21
R_B	4.88	4.76	4.31	4.40	5.02	5.28	5.04	5.19	5.27	3.63	4.17	5.53
R_M	2.82	3.19	-	2.74	4.21	-	4.02	4.76	-	4.26	-	-
χ^2	2.03	2.14	1.92	1.82	1.77	1.913	2.05	1.98	1.87	2.04	2.11	2.15
% Fe_2O_3	3.6(2)	3.6(2)	3.8(2)	3.5(2)	3.4(2)	3.6(2)	2.9(2)	2.7(2)	3.0(2)	2.3(2)	2.5(2)	2.5(2)

Table 3. Polyhedral analysis of LBFCO samples (*x*-concentration of Cr, $\delta-$ cation shift from centroid, ξ-average bond distance and bond-length variance, *V*- polyhedral volume, Δ-polyhedral volume distortion).

Cation	x	*T*(K)	δ(Å)	ξ(Å)	*V* (Å^3)	Δ	Valence
		4	0.220(2)	2.639+/- 0.218(1)	34.09(3)	0.097(3)	
	0.1	295	0.224(2)	2.643+/-0.212(1)	34.22(3)	0.098(3)	2.89(3)
		900	0.238(3)	2.666+/-0.214(1)	34.92(4)	0.104(4)	
		4	0.219(2)	2.638+/-0.204(1)	33.89(3)	0.099(3)	
La/Bi	0.25	295	0.217(2)	2.641+/-0.204(1)	33.91(3)	0.101(3)	2.86(3)
(c.n.=9)		900	0.235(3)	2.665+/-0.192(1)	34.72(4)	0.105(4)	
		4	0.217(2)	2.648+/-0.199(1)	34.16(3)	0.102(3)	
	0.5	295	0.220(2)	2.637+/-0.193(1)	33.79(3)	0.101(3)	2.87(3)
		900	0.219(3)	2.660+/-0.177(1)	34.51(4)	0.104(4)	
		4	0.215(2)	2.629+/-0.186(1)	33.36(3)	0.103(3)	
	0.75	295	0.216(2)	2.633+/-0.183(1)	33.50(3)	0.104(3)	2.88(3)
		900	0.231(3)	2.659+/-0.178(1)	34.24(4)	0.110(4)	
		4	0	2.007+/-0.034(1)	10.72(1)	0.006(1)	
	0.1	295	0	2.007+/-0.024(1)	10.74(1)	0.005(1)	2.87(3)
		900	0	2.017+/-0.033(1)	10.89(2)	0.006(2)	
		4	0	1.999+/-0.007(1)	10.64(1)	0.001(1)	
Fe/Cr	0.25	295	0	2.001+/-0.011(1)	10.67(1)	0.001(1)	2.94(2)
(c.n.=6)		900	0	2.008+/-0.018(1)	10.76(2)	0.003(2)	
		4	0	1.991+/-0.015(1)	10.51(1)	0.001(1)	
	0.5	295	0	1.992+/-0.014(1)	10.52(1)	0.002(1)	2.99(2)

	900	0	1.999+/-0.020(1)	10.63(2)	0.002(2)	
	4	0	1.980+/-0.028(1)	10.34(1)	0.001(1)	
0.75	295	0	1.982+/-0.031(1)	10.36(1)	0.002(1)	3.04(2)
	900	0	1.986+/-0.023(1)	10.43(2)	0.002(2)	

Table 4. Results of the symmetry analysis for the $k = 0$ magnetic propagation vector and Fe^{3+}/Cr^{3+} cations at the *4b* position of s.g. *Pnma*. There are four Fe/Cr sites which are: *1* = (0, 0, 0.5), *2* = (0.5, 0, 1), *3* = (0, 0.5, 0.5), *4* = (0.5, 0.5, 1). Definition of the magnetic modes, using the four Fe/Cr sites are *F*(++++), *G*(+−−+), *C*(+−+−), and *A*(++−−).

IR	Fe/Cr(4b)
Γ1	(*Gx, Cy, Az*)
Γ2	(*Cx ,Gy, Fz*)
Γ3	(*Fx, Ay, Cz*)
Γ4	(*Ax, Fy, Gz*)

Table 5. Summary of mode decomposition of the LBFCO compounds with *Pnma* structure, indicating the amplitude of all possible distortion components at 295 K.

Mode	Subgroup	Amplitude (Å)			
		x = 0.1	**x = 0.25**	**x = 0.5**	**x = 0.75**
R4+	*Imma*	0.13	0.08	0.09	0.08
R5+	*Imma*	0.63	0.60	0.59	0.57
X5+	*Cmcm*	0.18	0.17	0.16	0.14
M2+	*P4/mbm*	0.36	0.38	0.34	0.31
M3+	*P4/mbm*	0.02	0.02	0.02	0.05

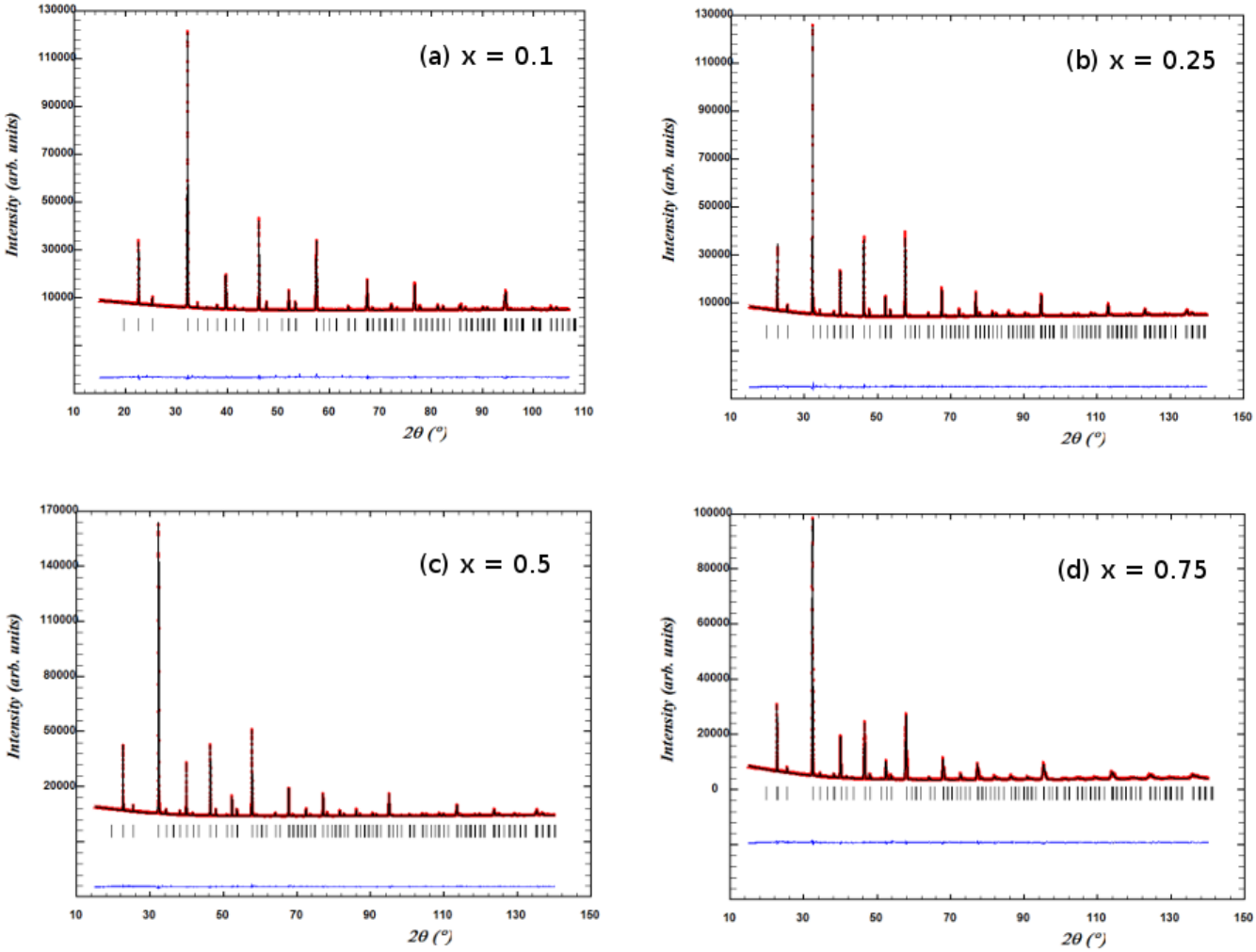

Figure 1.

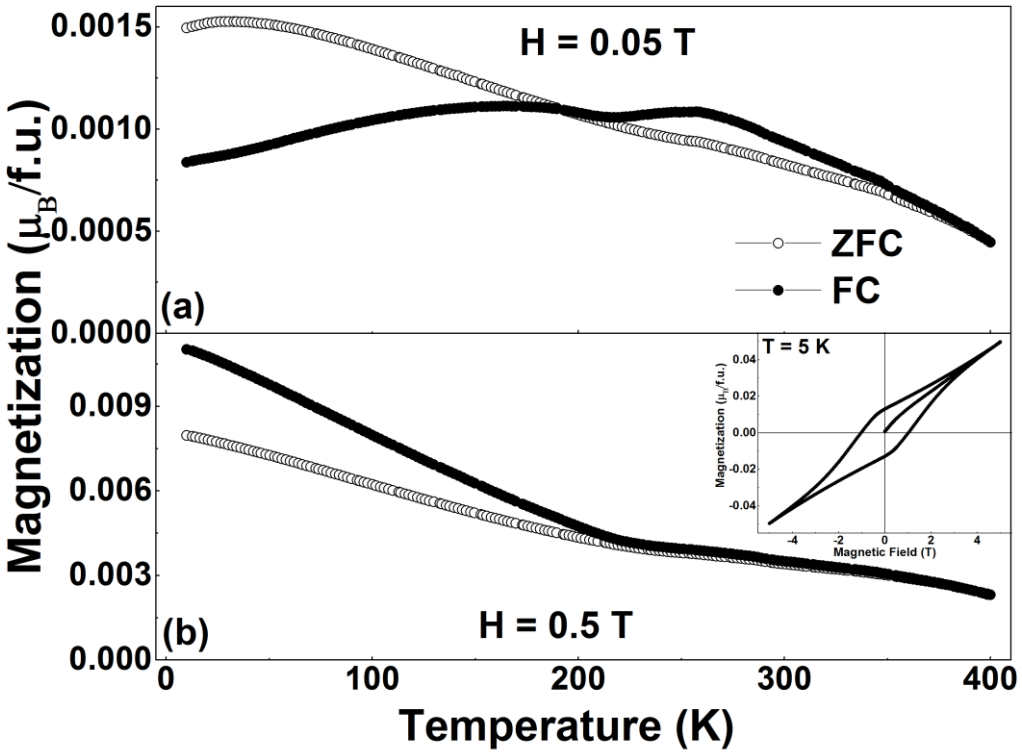

Figure 2.

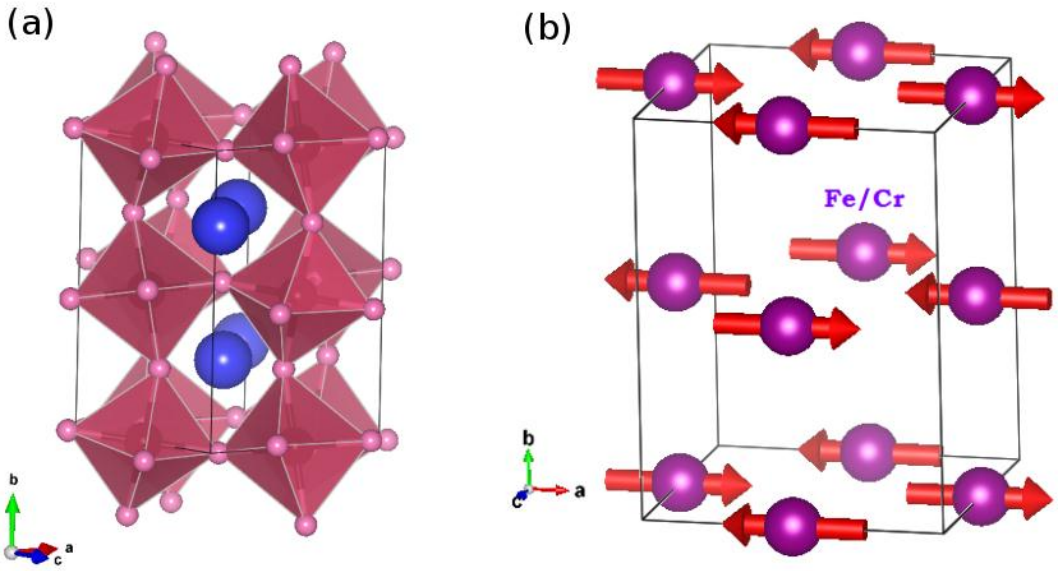

Figure 3.

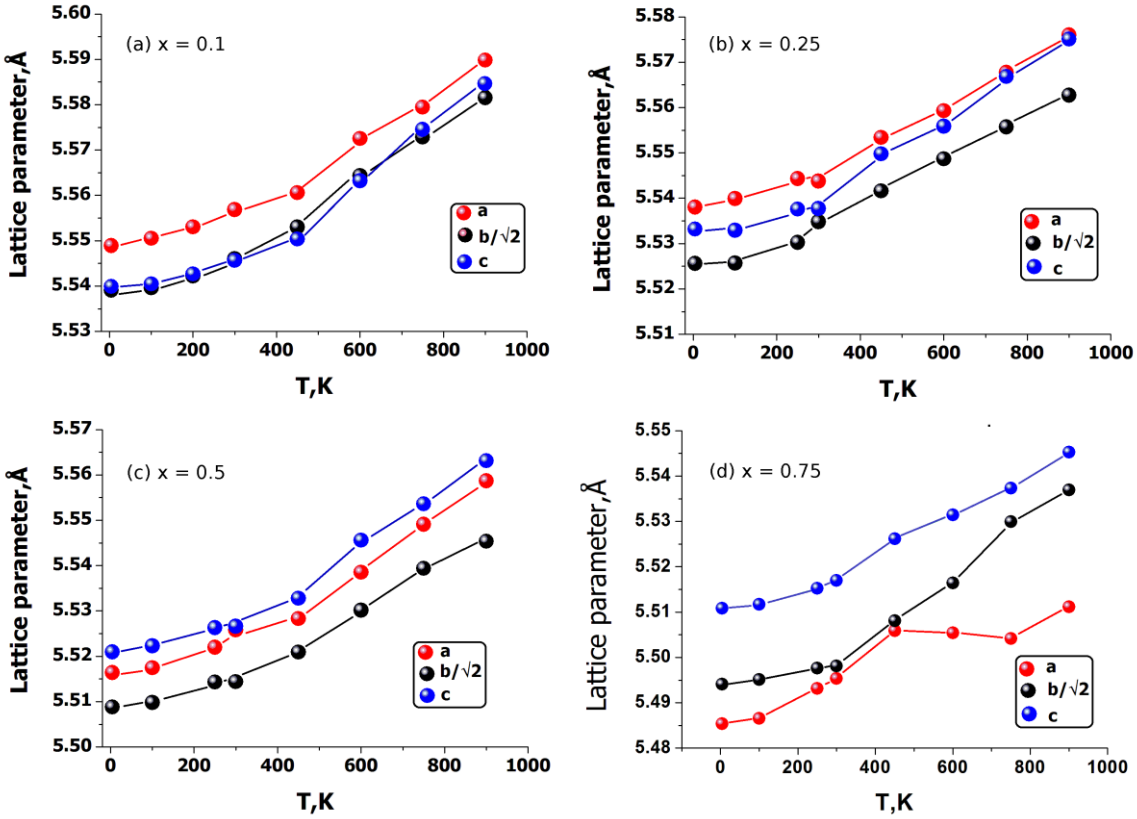

Figure 4.

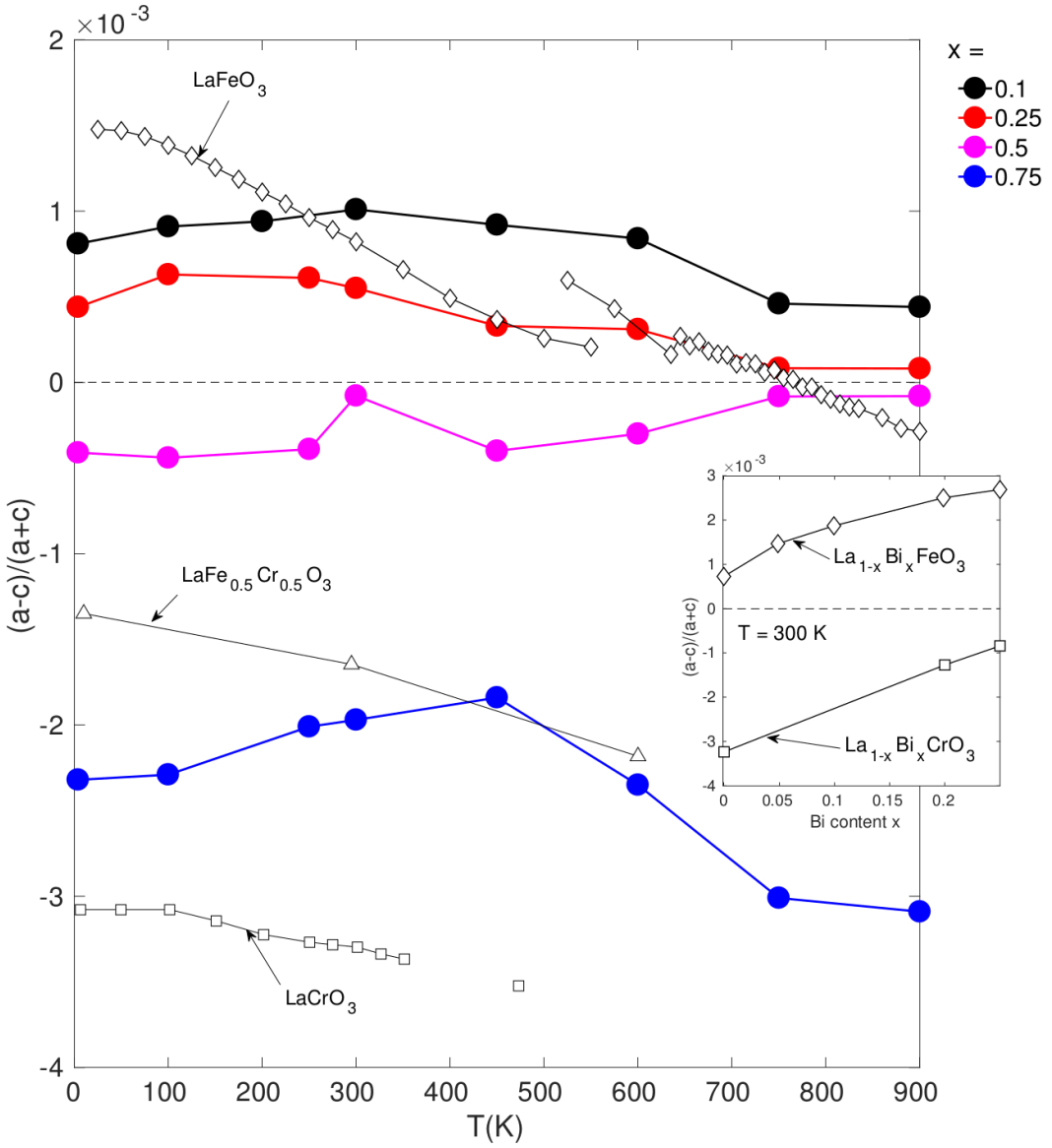
×10 -3
2
1
0
-1
-2
-3
-4
(a-c)/(a+c)
LaFeO3
LaFe0.5Cr0.5O3
LaCrO3
0
100
200
300
400
500
600
700
800
900
T(K)
X =
0.1
0.25
0.5
0.75
×10 -3
La1-xBixFeO3
T = 300 K
La1-xBixCrO3
(a-c)/(a+c)
0
0.05
0.1
0.15
0.2
Bi content x

Figure 5.

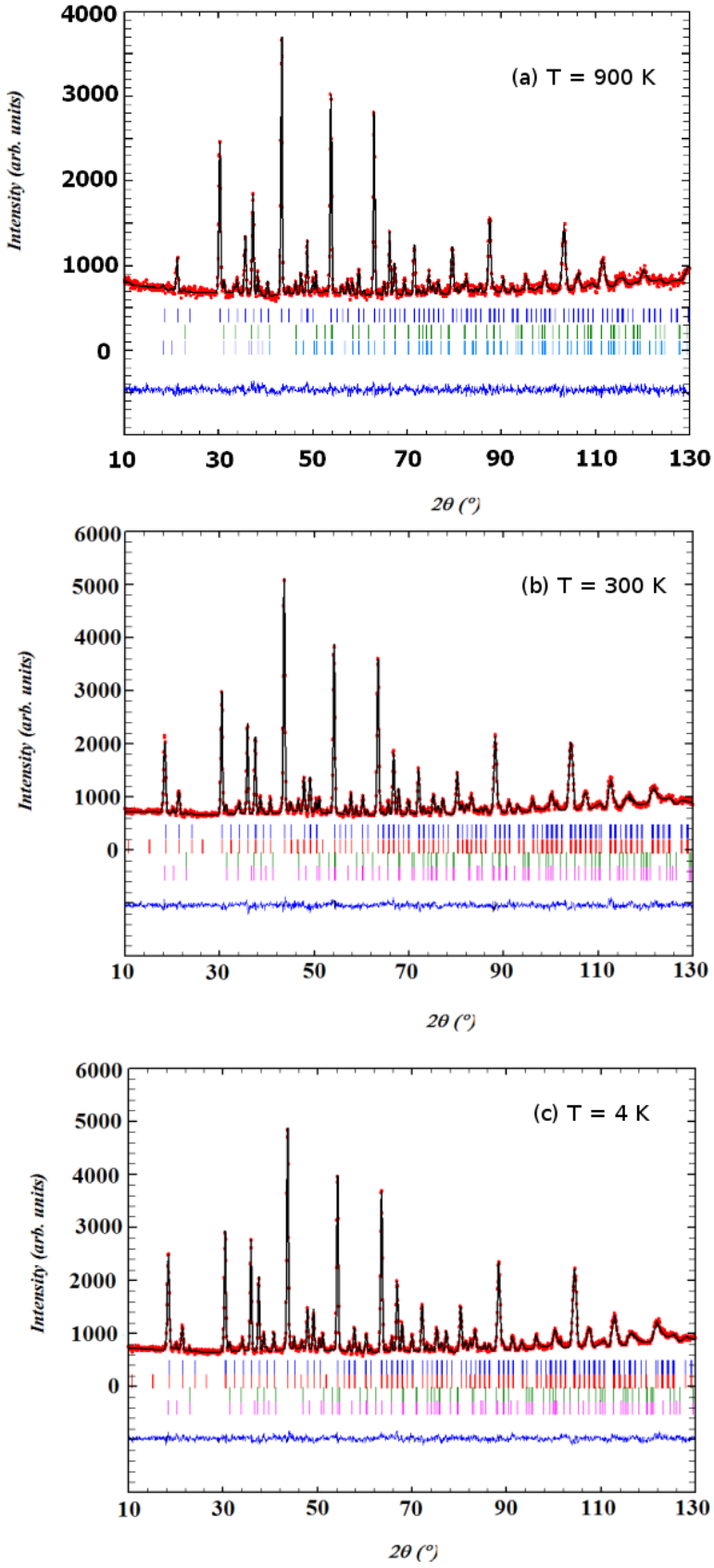
(a) T = 900 K
Intensity (arb. units)
2θ (°)
(b) T = 300 K
Intensity (arb. units)
2θ (°)
(c) T = 4 K
Intensity (arb. units)
2θ (°)

Figure 6.

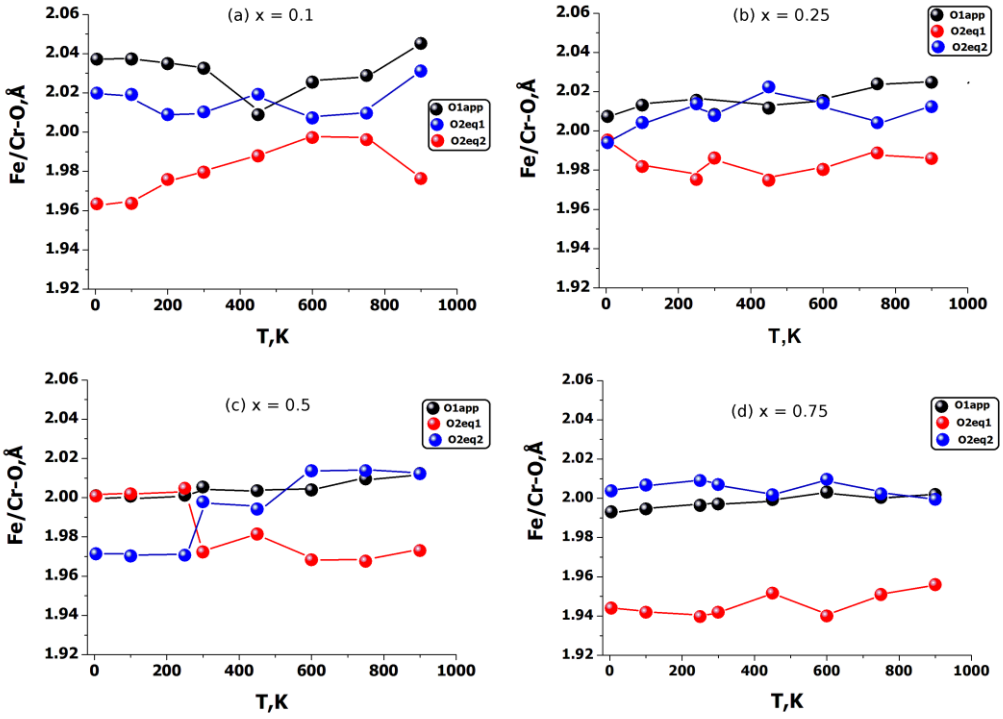

Figure 7.

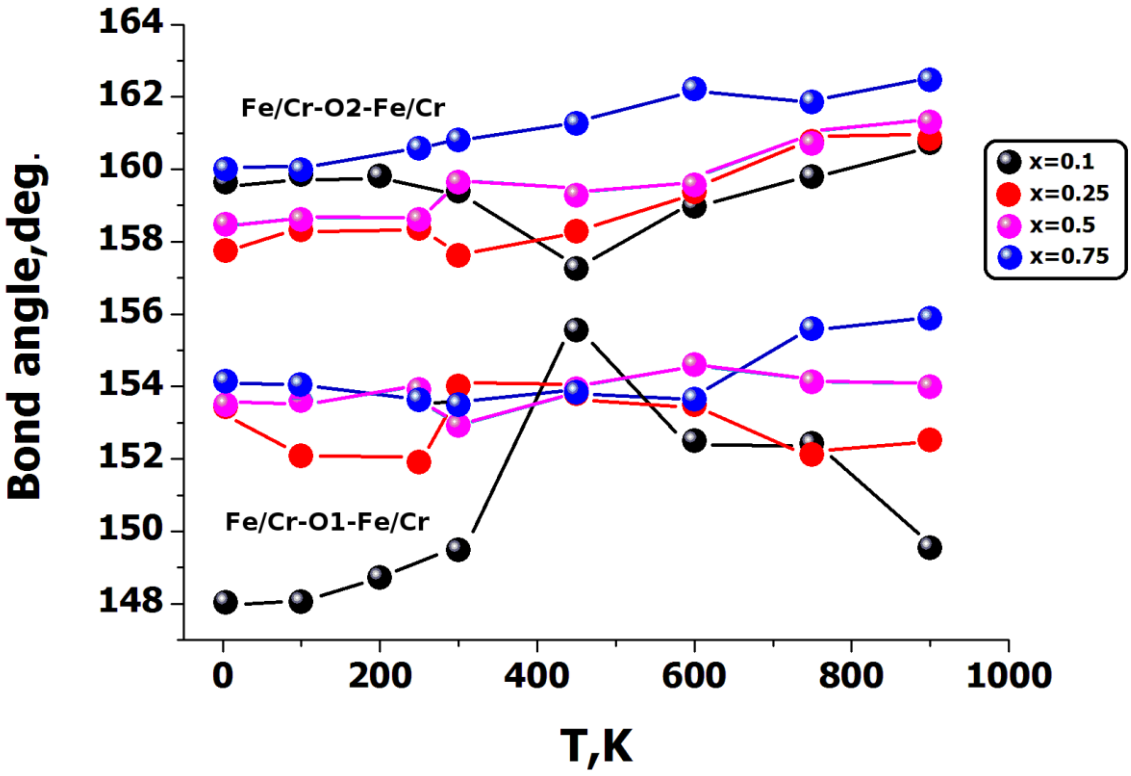

Figure 8.

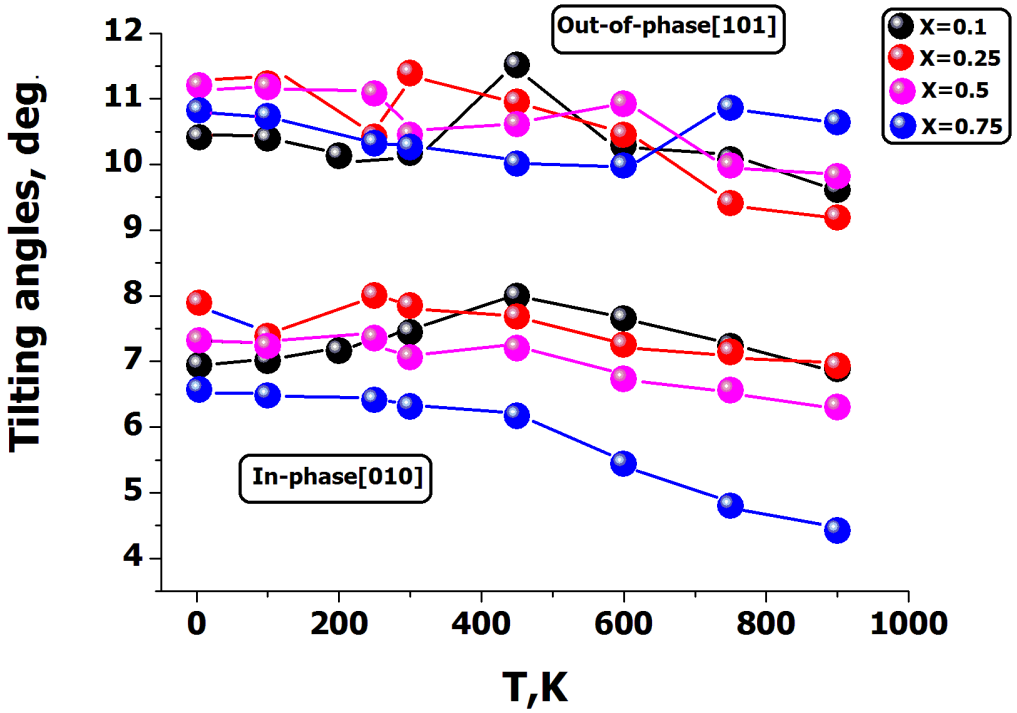

Figure 9.

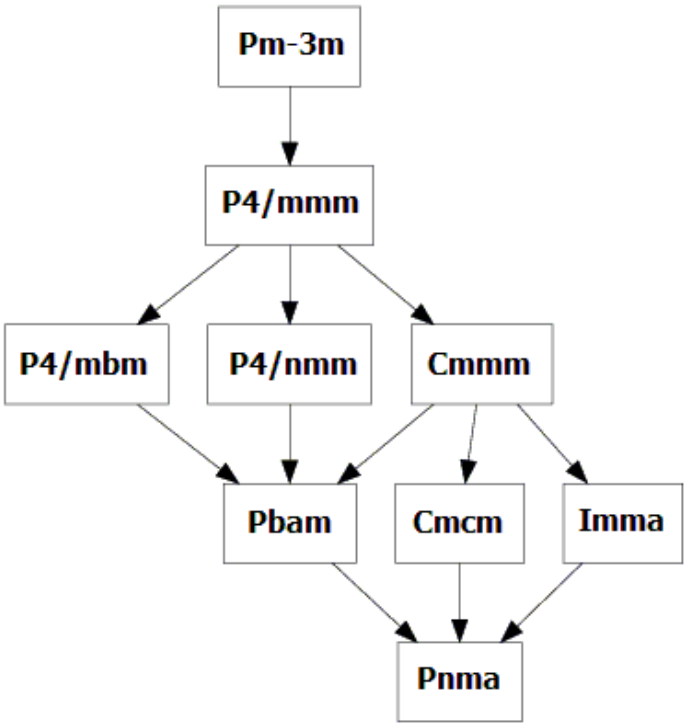

Figure 10.

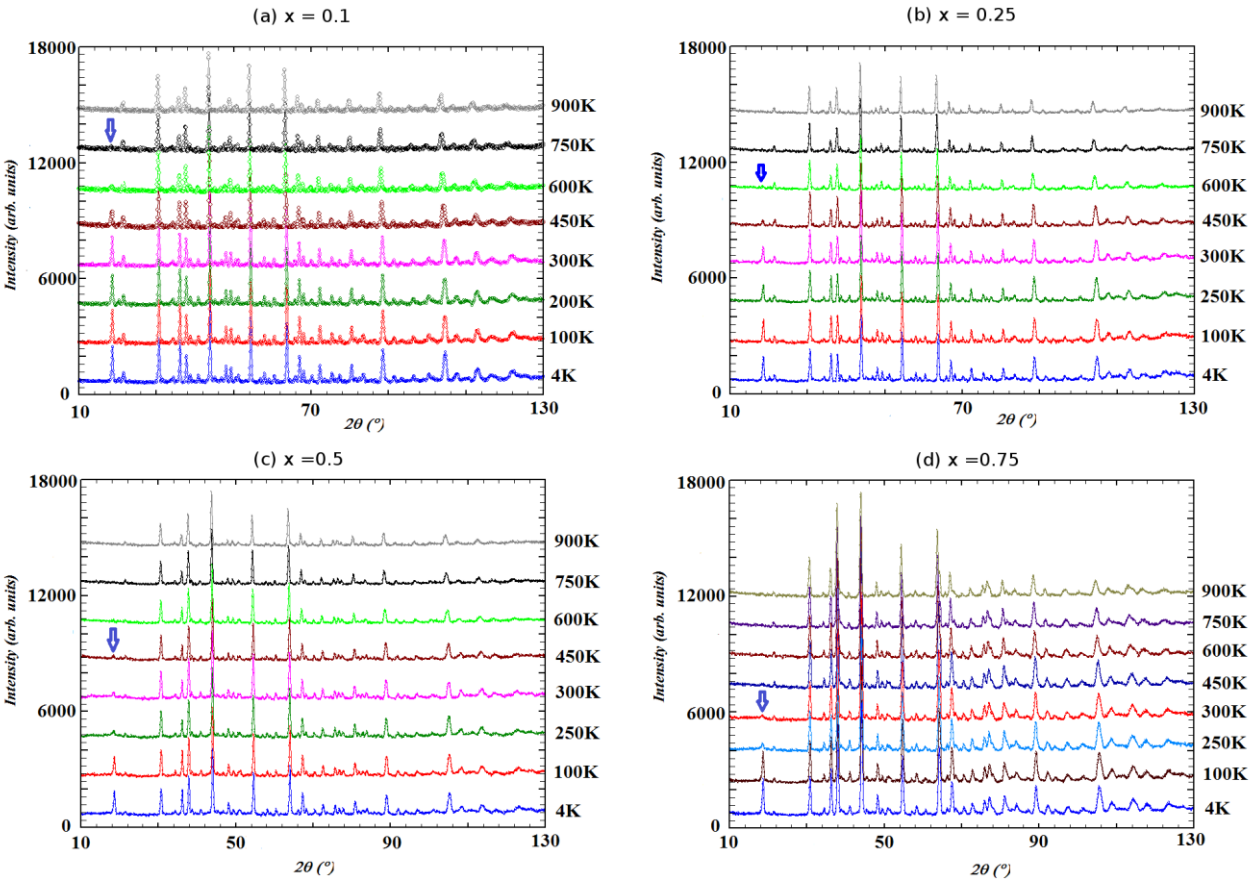

Figure 11.

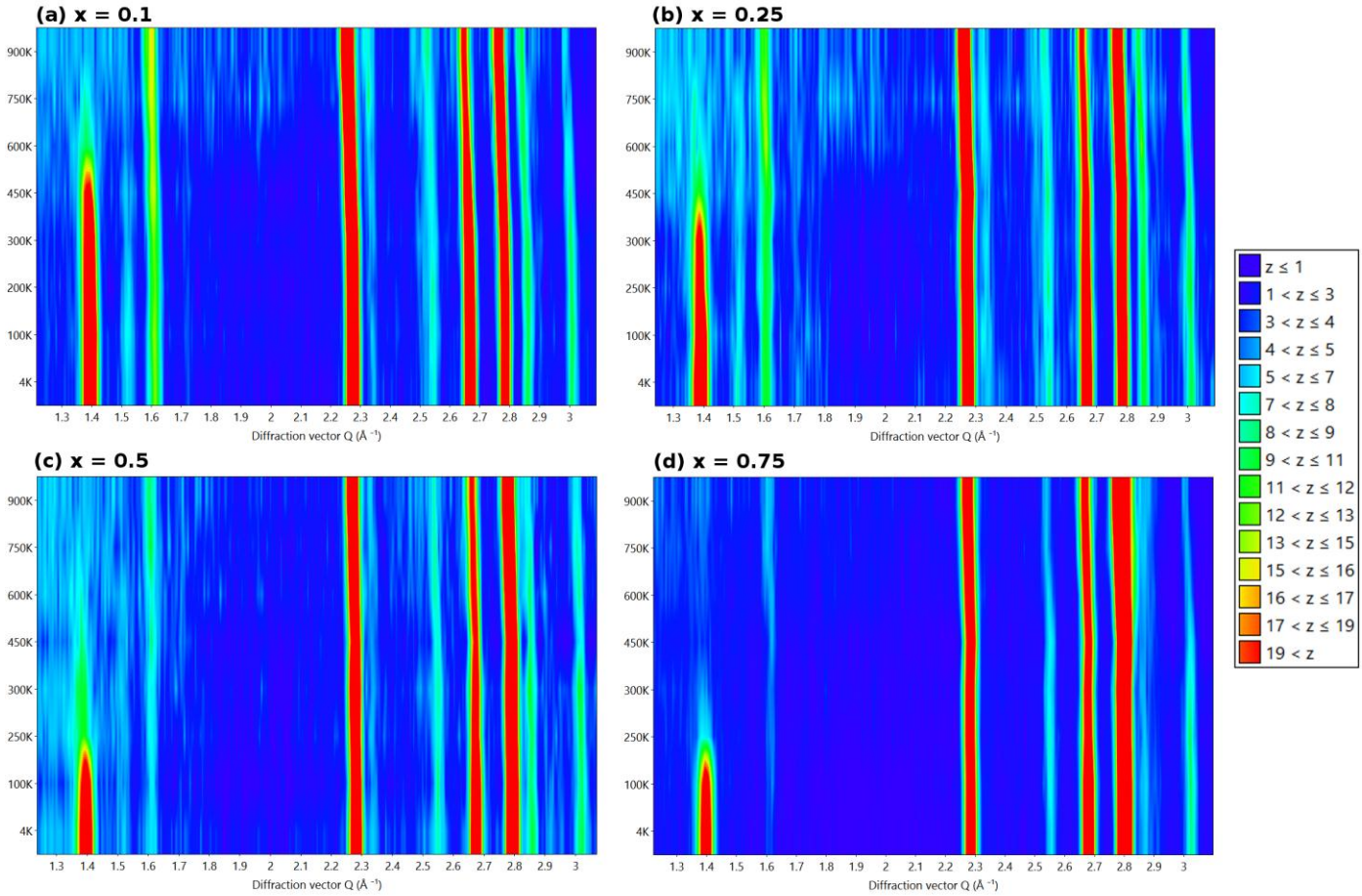

Figure 12.

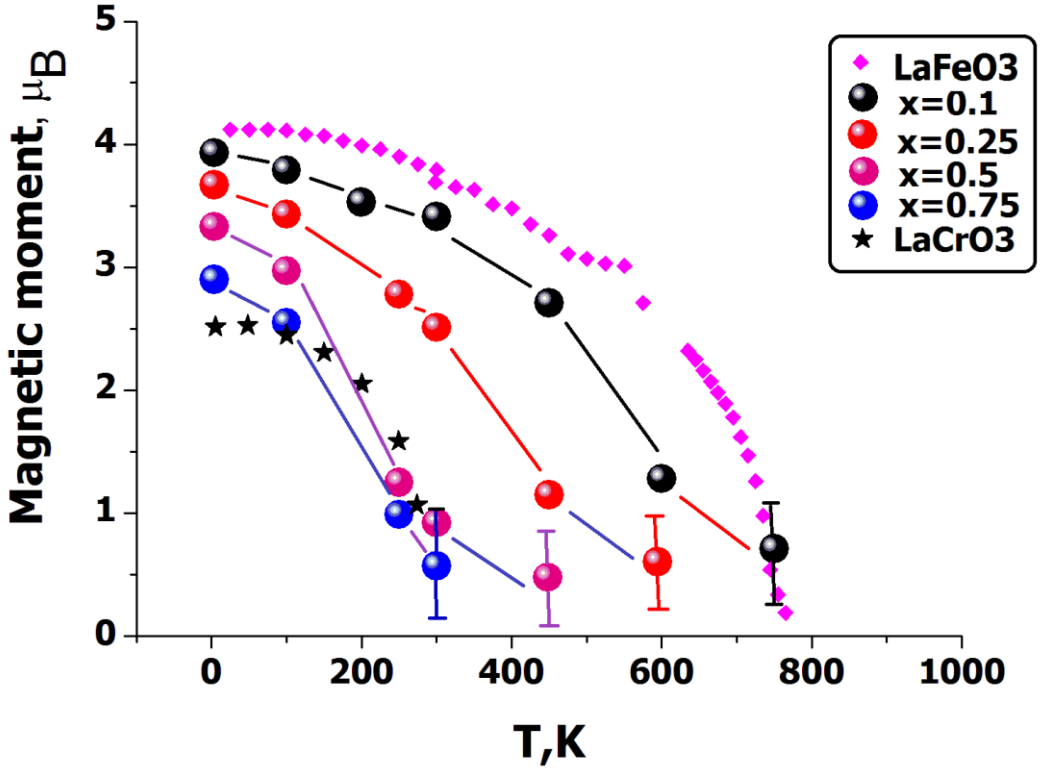

Figure 13.

Highlights

- The structural and magnetic properties of $La_{0.75}Bi_{0.25}Fe_{1-x}Cr_xO_3$ were investigated.
- The solid solutions were investigated by XRPD and NPD, and squid magnetometry.
- Fe^{3+} and Cr^{3+} ions were found to be randomly distributed on the perovskite B-site.
- The temperature and Cr concentration dependence of structural distortion was studied.
- Magnetic structures and magnetic transition temperatures were determined.